INDEX COPERNICUS INTERNATIONAL

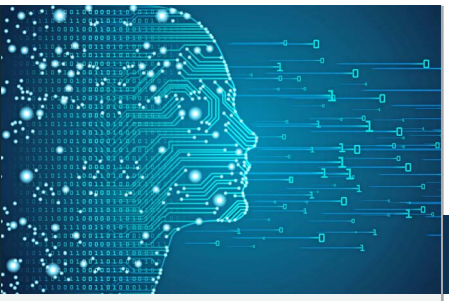

Bio-Algorithms and Med-Systems

WWW.BAMSJOURNAL.COM ISSN: 1896-530X

ORIGINAL ARTICLE

Received: 25.11.2024
Accepted: 27.12.2024
Published: 27.12.2024

CITE THIS ARTICLE AS:
Das M, Bayerlein R, Sharma S, Parzych S, Niedzwiecki S, Badawi RD, et al. "Development of correction techniques for the J-PET scanner," Bio-Algorithms and Med-Systems vol. 20, no. 1, pp. 101-110, 2024, DOI: 10.5604/01.3001.0054.9362

AUTHORS' CONTRIBUTION:
A. Conceptualization
B. Data Curation
C. Formal Analysis
D. Funding Acquisition
E. Investigation
F. Methodology
G. Project Administration
H. Resources
I. Software
J. Supervision
K. Validation
L. Visualization
M. Writing – Original Draft
N. Writing – Review & Editing

CORRESPONDING AUTHOR:
Manish Das; Faculty of Physics, Astronomy and Applied Computer Science, Jagiellonian University, Kraków; Łojasiewicza str. 11, 30-348 Kraków, Poland; E-mail: manish.das@doctoral.uj.edu.pl
Reimund Bayerlein; Department of Radiology, University of California Davis, Sacramento, California, United States;
E-mail: rbayerlein@ucdavis.edu

Development of correction techniques for the J-PET scanner

Manish Das[1,2,3ABCEFGIJKLMN], Reimund Bayerlein[4,5ABCEFGIJKLMN], Sushil Sharma[1,2,3ABEHJKMN], Szymon Parzych[1,2,3EN], Szymon Niedźwiecki[1,2,3EN], Ramsey D. Badawi[4,5EN], Ermias Yitayew Beyene[1,2,3EN], Neha Chug[1,2,3EN], Catalina Curceanu[6EN], Eryk Czerwiński[1,2,3EN], Kavya V. Eliyan[1,2,3EN], Bogusław Głowa[7EN], Alicja Hubalewska-Dydejczyk[7EN], Krzysztof Kacprzak[1,2,3EN], Tevfik Kaplanoglu[1,2,3EN], Kamila Kasperska[1,2,3EN], Grzegorz Korcyl[1,2,3EN], Aleksander Khreptak[1,2,3EN], Karol Kubat[1,2,3EN], Deepak Kumar[1,2,3EN], Edward Lisowski[8EN], Filip Lisowski[8EN], Justyna Mędrala-Sowa[1,2,3EN], Simbarashe Moyo[1,2,3EN], Wiktor Mryka[1,2,3EN], Marta Opalińska[7EN], Piyush Pandey[1,2,3EN], Martin Rädler[1,2,3EN], Magdalena Skurzok[1,2,3EN], Anna Sowa-Staszczak[7EN], Benjamin A. Spencer[4EN], Pooja Tanty[1,2,3EN], Keyvan Tayefi Ardebili[1,2,3EN], Anoop K. Venadan[1,2,3EN], Ewa Ł. Stępień[1,2,3DEGHJN], Paweł Moskal[1,2,3ABDEGHJKMN]

[1]Faculty of Physics, Astronomy and Applied Computer Science, Jagiellonian University, Kraków, Poland
[2]Total-Body Jagiellonian-PET Laboratory, Jagiellonian University, Kraków, Poland
[3]Center for Theranostics, Jagiellonian University, Kraków, Poland
[4]Department of Radiology, University of California Davis, Sacramento, California, United States
[5]Department of Biomedical Engineering, University of California Davis, Davis, California, United States
[6]INFN, Laboratori Nazionali di Frascati, Frascati, Italy
[7]Chair and Department of Endocrinology, Jagiellonian University Medical College, Kraków, Poland
[8]Cracow University of Technology, Kraków, Poland

ABSTRACT

Objective: Positron emission tomography (PET) is a widely used medical imaging technique that allows for non-invasive imaging of metabolic processes. However, traditional PET scanners rely on costly inorganic scintillators that limit their accessibility, especially in light of emerging long axial field-of-view devices. The modular J-PET scanner, an innovative alternative, uses 50-cm-long plastic scintillator strips, offering a cost-effective and modular solution. In this study we develop and assess the PET data correction techniques required for quantitative image reconstruction.
Methods: We present methods for attenuation correction, random coincidence correction using the delayed time window (DTW) technique and scatter correction based on Monte Carlo simulations. Phantom studies using the NEMA IQ phantom were performed to qualitatively evaluate these corrections.
Results: The results demonstrate that our implemented corrections for attenuation and random and scattered coincidences successfully improve the uniformity of tracer

distribution in homogenous volumes and significantly reduce undesired activity in cold regions. Despite limitations in sensitivity and axial resolution, the applied correction techniques effectively enhance image quality, providing promising results for future applications.

Conclusions: These findings highlight the potential of the modular J-PET system to offer affordable PET imaging and to pave the way for a total-body PET scanner based on plastic scintillators. Future work will focus on quantitative validation and the implementation of these corrections for human subject imaging.

KEYWORDS

positron emission tomography (PET), data corrections, nuclear medicine imaging, plastic scintillator, J-PET, large AFOV

LIST OF ABBREVIATIONS

^{18}F – fluorodeoxyglucose
CASToR – Customizable and Advanced Software for Tomographic Reconstruction
CT – computed tomography
CTW – coincidence time window
DTW – delayed time window
FOV – field of view
FPGA – field-programmable gate array
FWHM – full width at a half-maximum
HU – Hounsfield Units
J-PET – Jagiellonian positron emission tomography
LAFOV – large axial field-of-view
LOR – lines of response
LYSO – lutetium-yttrium oxyorthosilicate
MC – Monte Carlo
NEMA – National Electrical Manufacturers Association
PET – positron emission tomography
SiPMs – silicon photomultipliers
SSRB – single scatter randoms background
SSS – single scatter simulation
TOF – time-of-flight

BRIEF DESCRIPTION OF THE WORK

This work focuses on developing PET data correction techniques for a cost-effective modular J-PET scanner that uses plastic scintillators. Methods for attenuation, random and scatter corrections were developed and qualitatively validated using a NEMA IQ phantom, showing improvements in image quality by enhancing tracer uniformity and reducing artifacts. These findings highlight J-PET's potential for affordable PET imaging, with future work aimed at the implementation of the correction techniques for human subject imaging and total-body J-PET applications.

INTRODUCTION

Positron emission tomography (PET) is a widely utilized medical imaging technique recognized for its diagnostic precision and versatility, with applications spanning physiological studies, brain function analysis, drug delivery tracking and metabolic activity assessment. The administration of a radioactive positron-emitting tracer into the human body allows for molecular 3D-imaging of metabolic processes. As a result, photons with an energy of 511 keV are emitted and captured with a ring of scintillation detectors and used for tomographic image reconstruction. However, traditional PET scanners rely on costly inorganic scintillators and a radial detector arrangement that demands a substantial number of electronic components. Together, the expense of the crystals and the extensive electronics significantly increase the overall cost of conventional PET systems, limiting their accessibility [1, 2]. The J-PET (Jagiellonian positron emission tomography) scanner represents an innovative alternative utilizing elongated polymer scintillator strips, facilitating the creation of economical and durable standalone detection units [3–6]. The modular J-PET scanner is a portable and lightweight device weighing 60 kg. It consists of 24 independent detector modules configured in a regular 24-sided polygon with a diameter of 73.9 cm [7]. Each module contains an array of 13 axially aligned, 50-cm-long plastic scintillators connected to silicon photomultipliers (SiPMs) and front-end electronics at both ends. The 511-keV photons interact within the scintillator strips predominantly through the Compton effect, producing scintillation photons [8, 9]. Scintillation light is detected using silicon photomultipliers, which are subsequently processed utilizing FPGA-based data capture in a triggerless mode [10, 11].

Following the standards set by the National Electrical Manufacturers Association (NEMA), the performance characteristics of the modular J-PET were assessed in the previous studies. The average system sensitivity was determined to be 0.768 ± 0.003 cps/kBq at the centre, with a peak sensitivity of 2.1 cps/kBq [12, 13]. The experimental spatial resolution for time-of-flight (TOF) image reconstruction was 4.92 ± 0.56 mm, 7.38 ± 0.51 mm and 30.73 ± 0.52 mm FWHM in radial, tangential and axial direction, respectively. The radial spatial resolution value was similar to those of commercial PET devices [14]. The scatter fraction, calculated via single scatter randoms background (SSRB) algorithms, was 41.7 ± 0.2%. The TOF resolution of the modular J-PET was reported as 628 ps FWHM [12, 13].

One crucial goal of PET imaging is the quantification of the activity concentration in every image voxel in the field of view (FOV). The precision of these estimates is dependent on the accurate identification of detected photon coincidences as genuine coincidences, and on the other hand the correction of certain physical processes that degrade image quality. Various factors may lead to inaccuracies in the estimation process. The most important of these is generally the attenuation (i.e., absorption) of photons traveling through the object (e.g., the human subject), which leads to an underestimation of tracer concentration in deeper tissues. The J-PET utilizes a CT-based attenuation correction method to resolve this issue.

Coincidence events in PET imaging can be divided into three types (Fig. 1.). True coincidences arise when both photons from a single annihilation event are detected by the detector pair (Fig. 1A.). These events yield dependable data, crucial for the precise quantification of radiopharmaceutical concentration and image quality.

A further source of error in PET imaging – and also the second type of coincident event – is random coincidences, which occur when two unrelated photons from different annihilations are detected within the same coincidence time window (CTW). Random coincidences cause an additional unwanted apparent activity concentration in the reconstructed image and increase the background bias, thereby preventing the precise estimation of radiopharmaceutical concentrations (Fig. 1B.). Various methods can be employed to account for random coincidences, such as the singles rate method [15–17], delayed time window (DTW) method [15, 17, 18], and singles prompts method [19]. The delayed time window method was utilized in the J-PET system to tackle this issue.

Being the third type of coincidence, scattered photons cause major challenges for PET imaging: when photons scatter once or multiple times inside the object in the FOV, the resulting line of response (LOR) does not generally contain the source location (Fig. 1C.). This causes a degradation of image quality, introduces biases and reduces contrast. To address this, reliable scatter correction techniques are crucial. One commonly used technique is single scatter simulation (SSS) [20], which analytically estimates the contribution of scatter to every LOR. However, SSS may become inaccurate for oblique lines of response, in which the probability for multiple scatter increases. To improve this, Monte Carlo-based techniques have been developed [21] to simulate all possible photon interactions within the tissue. Although these methods require more computational power they may provide better scatter correction, especially in large axial field-of-view (LAFOV) scanners such as the uEXPLORER [22], where multiple scattering is more likely due the larger number of oblique LORs. To address the scatter correction for J-PET, a Monte Carlo-based scatter correction method was developed and implemented to enhance accuracy based on Bayerlein et al. (2024) [23].

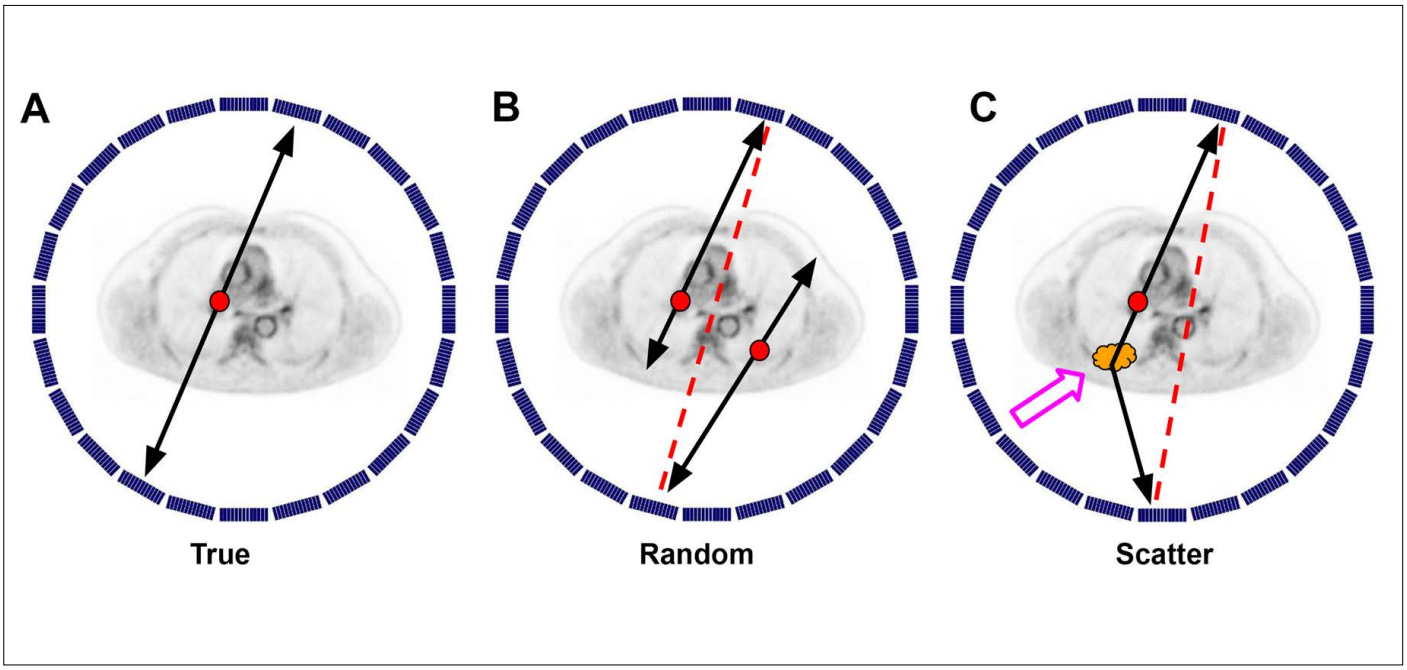

Fig. 1. Illustration of the three primary types of coincidences detected by the PET system: true, random and scatter coincidences. (A) True coincidences, where both photons originate from the same annihilation event and are detected without scattering inside the object in the FOV; (B) Random coincidences, where two photons are detected that originate from separate, unrelated coincidences; (C) Scatter coincidences, where one or both photons undergo scattering before detection.

In the following, we will present the data correction methods for J-PET to compensate for attenuation and for random and scattered coincidences. We will show the first qualitative results using phantom data.

METHODS

Phantom Study

To visualize and evaluate the implemented data corrections the NEMA IQ phantom was used, which consists of 6 spheres of 10 mm-, 13 mm-, 17 mm-, 22 mm-, 28 mm and 37 mm-diameter filled with water with a high activity concentration of the radiotracer fluorodeoxyglucose [^{18}F] FDG, suspended in a background with lower concentration. The sphere-to-background activity concentration ratio was 10:1. The lung insert was filled with Styrofoam balls. The phantom was placed on a plexiglass sheet with two wooden guiding rails on both sides and then pushed into the scanner bore. The measurement was conducted for a duration of 60 minutes, as depicted in Fig. 2A. The data was obtained through a triggerless acquisition system and analysed using the methods described in detail in the references [7]. The data are filtered for reconstruction by applying a CTW of 3-ns, an energy window, and requiring that two interactions from the same coincidences have an angular separation of more than 60 degrees in the trans-axial direction. This angular separation criterion helps reduce coincidences caused by scattering between detectors. After analysis with the J-PET framework, the total number of coincidences available for reconstruction was 40.38 million. Following the measurement with the J-PET, a CT image of the phantom was taken using the commercial GE Discovery MI Gen 2 PET/CT at Jagiellonian Medical University in Krakow, as shown in Fig. 2B. Fig. 2A. and 2B. illustrate that different beds were used for the J-PET and CT measurements performed at the Medical University of Krakow.

Attenuation Correction

The method used for attenuation correction in the J-PET system is based on CT-derived attenuation correction, as outlined by Carney et al. [24]. This approach involves converting Hounsfield Units (HU) from CT images into linear attenuation coefficients for 511-keV photons using bilinear interpolation. The bilinear transformation of HU to attenuation coefficients includes a breakpoint, or transition point, where the relationship between Hounsfield Units and the linear attenuation coefficients changes. The use of two different linear functions below and above the breakpoint ensures accurate conversion for both soft tissues and denser structures such as bone, and was therefore also used in this study. The resulting attenuation map was resampled to a grid size of 200 × 200 × 200 voxels, with each voxel measuring 2.5 x 2.5 x 2.5 mm^3, and Gaussian smoothing was subsequently applied using $\sigma = 2$ voxels, equivalent to 5 mm in physical units, to align with the resolution of the PET system. The smoothing is applied uniformly in all directions.

After generating, the attenuation map is merged with the sensitivity map, as shown in Fig. 3. This step is carried out within the CASToR framework using the SENS optimizer [25]. In this study the sensitivity map was derived entirely from a Monte Carlo (MC) simulation. The MC simulation consisted of a high-statistics acquisition of a uniform cylinder that filled the scanner's FOV completely.

Randoms Correction

The method employed for the random correction in this study is the delayed time window (DTW) technique [15]. This algorithm

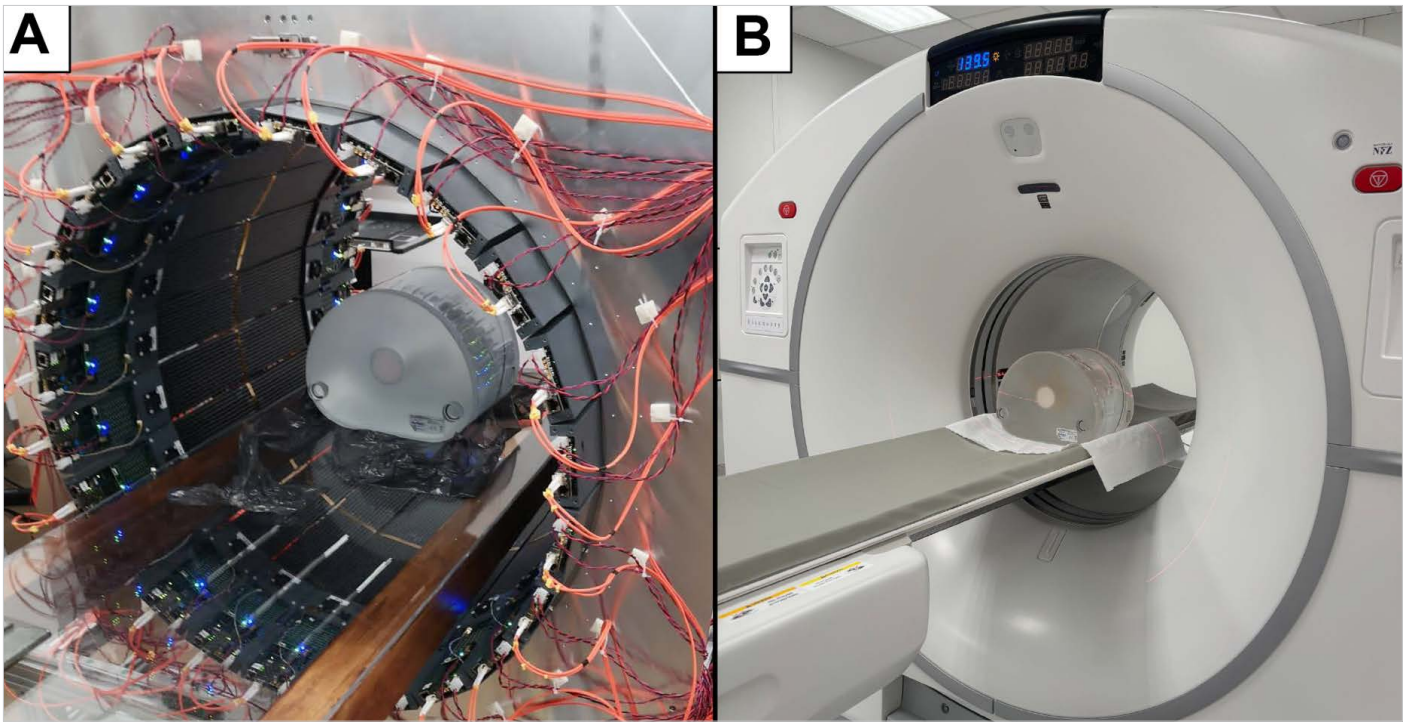

Fig. 2. (A) Measurement of the NEMA IQ phantom using the J-PET system at Jagiellonian University. The phantom was placed on a plexiglass plate with two wooden guiding rails; (B) CT measurement of the same NEMA IQ phantom on the GE Discovery MI Gen 2 system at the Medical University of Krakow, which was used for attenuation correction.

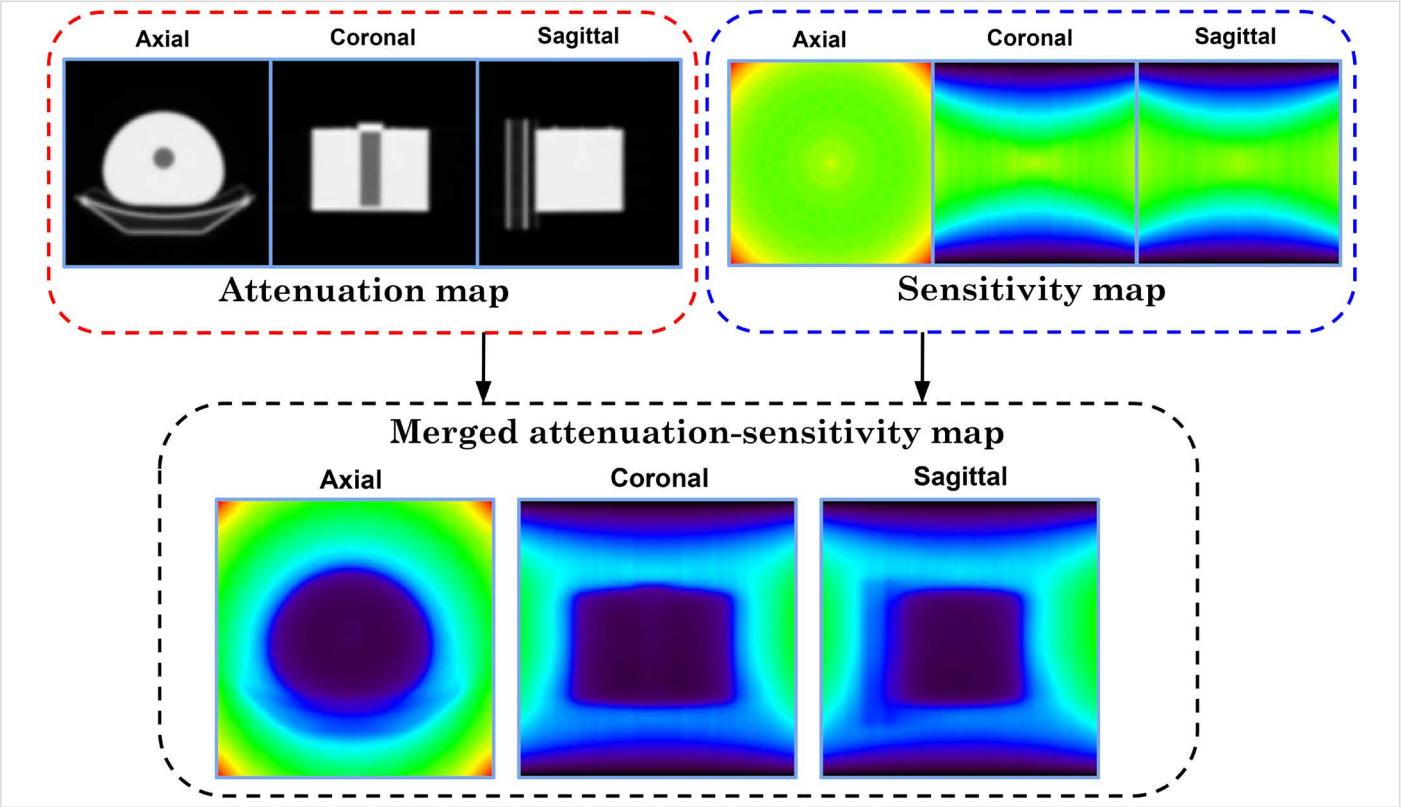

Fig. 3. Illustration of the process for merging the attenuation map of the NEMA IQ phantom with the sensitivity map derived from a Monte Carlo (MC) simulation. The merged map, created using the optimizer SENS from the CASToR software, combines both maps, ensuring accurate corrections during image reconstruction.

necessitates the preparation of coincidences within a time window that is offset from the initial interaction, typically requiring a second, parallel data acquisition. However, by utilizing the trigger-less acquisition of the J-PET, which captures each photon interaction individually, both pieces of information can be stored simultaneously. This eliminates the need for a separate delayed channel, which is commonly required in conventional PET scanners.

The J-PET detector consists of 24 modules, each containing 13 plastic scintillators, which adds up to 312 trans-axial scintillators. For image reconstruction each scintillator is virtually divided into 200 axial pseudo-crystals, resulting in a total of 62,400 pseudo--crystals in the scanner. Considering that for a valid coincidence two pseudo-crystal must be separated by at least 60 degrees in a transaxial direction, 208 pseudo-crystals can form coincidences at each projection angle. With interleaving there are 207 LORs per projection angle, and 156 angles and 200 x 200 possible detector planes. This results in 1,291,680,000 LORs in the entire scanner. High count rates would be required for a reliable estimate of the contribution of randoms to each LOR. To address the issue of low statistics in randoms correction, the scintillators are grouped into larger blocks combining eight pseudo-crystals along the axial direction and four pseudo-crystals along the trans-axial direction. With 51 block-based projection bins, 39 angles and 25 axial blocks, the total number of block pairs in the scanner is 1,243,125. Thus, the number of randoms collected in a block pair is three orders of magnitude higher than in a pseudo-crystal-based LOR.

For this study, a 3-ns CTW was used to register coincident annihilation events (prompt events). If there are more than two interactions within the CTW, the event is rejected in this analysis. To implement the DTW method for the estimation of the randoms rate, we took advantage of the triggerless data acquisition by introducing a delayed window of 100 ns after the registration of the first interaction. Following this delayed window, primarily a 3-ns delayed coincidence time window was used to search for a second single interaction, forming a delayed coincidence, as illustrated in Fig. 4. This ensured that the two registered interactions originated from two different annihilation events. Any events with more than one interaction in the delayed CTW were rejected in this analysis. Then the coincidence processor moved on to the next single interaction in the list mode data set, repeating the above coincidence search.

However, using a 3-ns delayed CTW resulted in high variance in random factors due to still very limited statistics even on block level. To mitigate this issue, the delayed CTW was increased to 30 ns, as shown in Fig. 4., improving statistics by a factor of 10. However, this adjustment still required further optimization of the J-PET system. After obtaining the random coincidences from the data, events were binned into block-based sinograms, as described above. The rate of the random coincidences contributing to LOR “i”, located in detector block pair b, was approximated following the assumption that there was a uniform distribution of randoms over all LORs in one block sinogram bin. The rate of the random coincidences contributing to LOR “i” could then be calculated as follows:

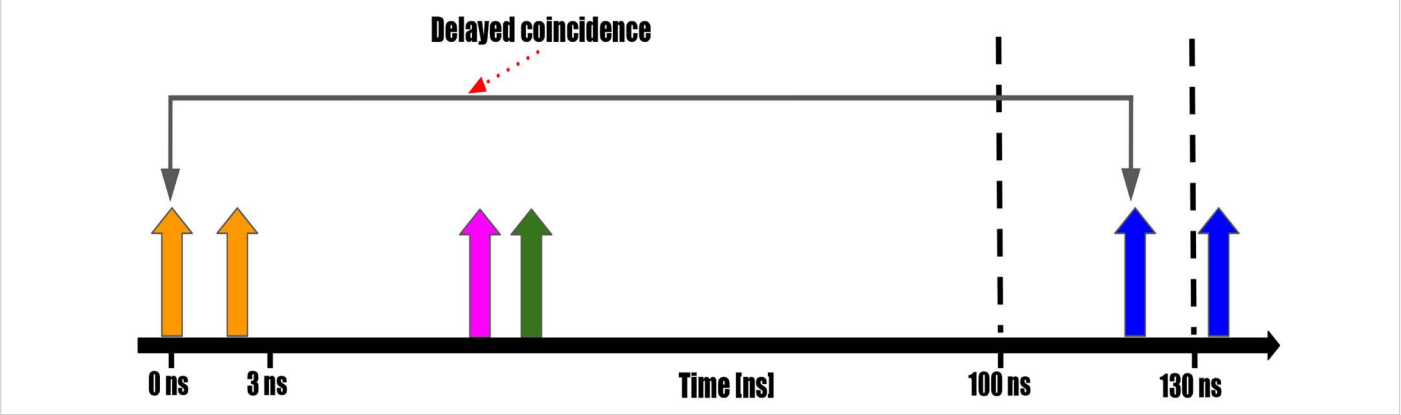

Fig. 4. Schematic of the delayed time window random correction method. The first interaction was recorded, and a 100-ns delayed time window was established, during which no subsequent interactions were accepted. Following this, a delayed coincidence time window of 30 ns was defined, within which a second interaction was accepted, forming a delayed coincidence. The pink and green arrows illustrate an example of a random coincidence accepted during the true coincidence search, resulting in a false coincidence. These interactions originated from different coincidences, with one interaction either undetected by the detector or attenuated within the object. The orange arrows within the first CTW constitute an example of a true coincidence. The time stamps shown in the image are not to scale and are provided for illustrative purposes only.

$$R_i = \frac{N_b}{N_{LOR} \times T_{meas} \times 10}$$

where N_b represented the number of entries in block sinogram bin b in the generated randoms sinogram, T_{meas} was the total measurement duration and $N_{LOR} = (8 \times 4)^2 = 1{,}024$ denoted the number of possible pseudo-crystal-based LORs between two detector blocks. The factor of 10 was required to compensate for the previously enlarged delayed CTW. After calculating the rate of random coincidences for each LOR, these rates were supplied to the list-mode data for CASToR.

Scatter Correction

The scatter correction method for the J-PET system was implemented following the Monte Carlo (MC)-based scatter correction technique, originally developed for the uEXPLORER by Bayerlein et al. (2024) [23]. This method employed the MC toolkit SimSET to simulate the J-PET scanner geometry. During the implementation, due to the limited availability of materials in the SimSET database, LYSO crystals were used as an approximation instead of plastic scintillators. This subsequently increased the sensitivity in the simulation and allowed for reduced run time. As in the randoms correction, the plastic scintillator strip was subdivided into 200 axial pseudo-crystals for the simulation. Consequently, the pseudo-crystals were also combined to blocks of four trans--axial and eight axial pseudo-crystals, and the collected simulated coincident events were sorted into block-based sinograms.

The simulated trues and scatter sinograms were scaled plane-by--plane to the measured randoms-corrected prompts sinograms. Gaussian smoothing was applied to the sinograms of a scaled--scattered sinogram with a smoothing kernel with a full width at a half-maximum (FWHM) of 4 bins. Similar to the randoms correction, the rate of scattered coincidences per LOR was calculated as follows:

$$S_{i,t} = \frac{S_{b,t}^{sim,Gauss} \times f_k}{N_{LOR} \times T_{meas}}$$

where $S_{b,t}^{sim,Gauss}$ is the number of entries in TOF bin t, and block sinogram bin b in the scaled and smoothed sinogram of simulated scattered coincidences. f_k denotes the scaling factor for plane k. The obtained scatter rate for each LOR and TOF bin was then supplied to the list mode of the CASToR to perform the reconstruction.

Image Reconstruction

Image reconstruction was performed with the CASToR software package [25]. The TOF list mode-ordered subset expectation maximization algorithm with four iterations with four subsets were used. The TOF resolution kernel was modelled as the Gaussian function. A raytracing projector, based on the incremental Siddon algorithm [26], was employed along each line of response, configured to use 10 rays. Additionally, the reconstruction process included image-based PSF modelling, integrated within the CASToR framework. This modelling applied a trans-axial FWHM of 3 mm, an axial FWHM of 30 mm and a Gaussian kernel with a 2-sigma value, in which the kernel's size was determined by two standard deviations (2σ) in both directions, respectively. The reconstructed image size was set at 200 × 200 × 200 voxels, with each voxel measuring 2.5 x 2.5 x 2.5 mm³. In addition to the correction techniques mentioned in the article, normalization was also applied during reconstruction, utilizing a component-based method [27, 28].

RESULTS

Attenuation Correction

Following the merging of the attenuation and sensitivity maps, image reconstruction was executed utilizing the CASToR framework with list-mode files obtained from the modular J-PET

system, employing the NEMA IQ phantom. Fig. 5. shows the images reconstructed with only the sensitivity map and with the merged sensitivity-attenuation map. It is evident that without attenuation correction there was an underestimation of tracer distribution in the deeper regions of the phantom compared to the edges. However, after applying attenuation correction, the tracer distribution appeared more uniform throughout the background region of the phantom.

Random Correction

In this measurement, a total of 74,005,689 random coincidences were acquired, with a delayed time window of 100 ns and a delayed CTW of 30 ns, as described in the previous section. To ensure accurate estimation of random coincidences, the delayed CTW was increased by a factor of 10, which implies that the effective number of random coincidences was approximately 7,400,568. For comparison, the total number of prompt coincidences recorded was 40,385,397. Therefore, the proportion of random coincidences in this measurement was about 18%. To illustrate the effectiveness of the random correction, Fig. 6. presents the relative difference between the non-random corrected and random corrected images. It provides a normalized measure of the extent to which random coincidences have been removed during the correction process, providing a clear measure of the improvement in image quality due to the random correction.

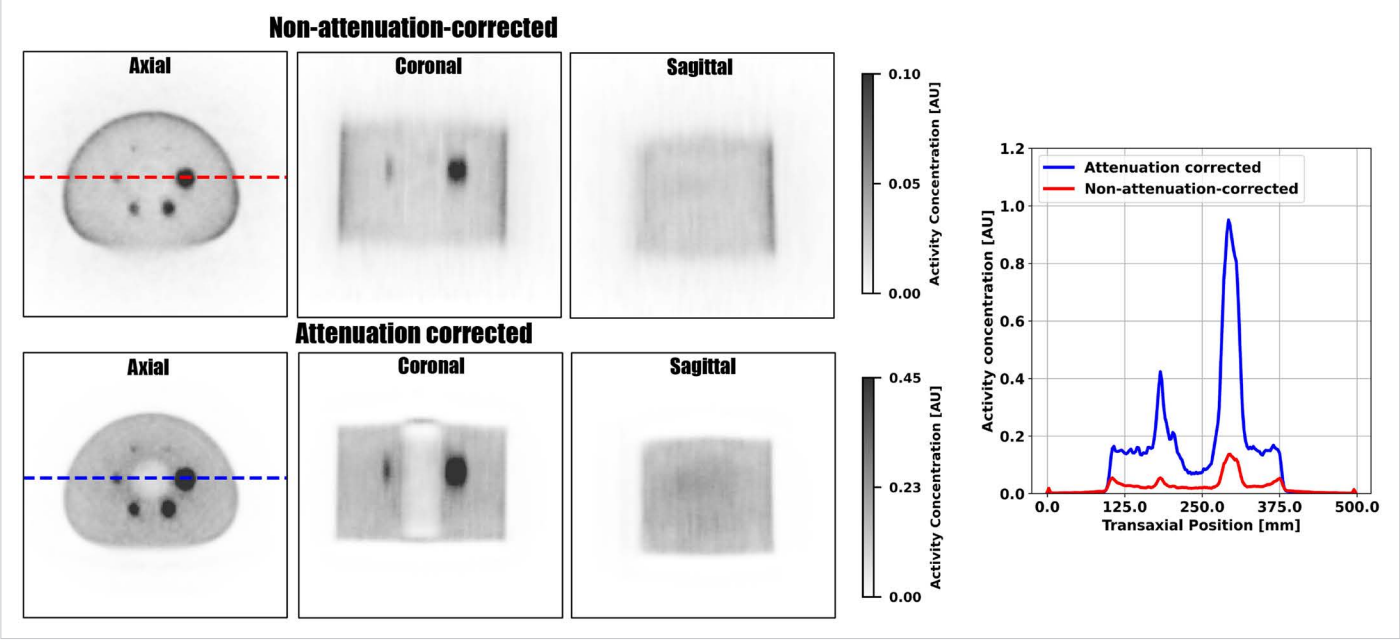

Fig. 5. Comparison of images of the NEMA IQ phantom without (top) and with (bottom) attenuation correction, along with line profiles. No scatter correction has been applied in these examples. The non-attenuation-corrected image shows an underestimation of tracer distribution in deeper parts of the phantom, resulting in reduced signal in these areas. "Attenuation correction" compensates for this underestimation, providing a more homogenous and more accurate representation of tracer distribution across the phantom.

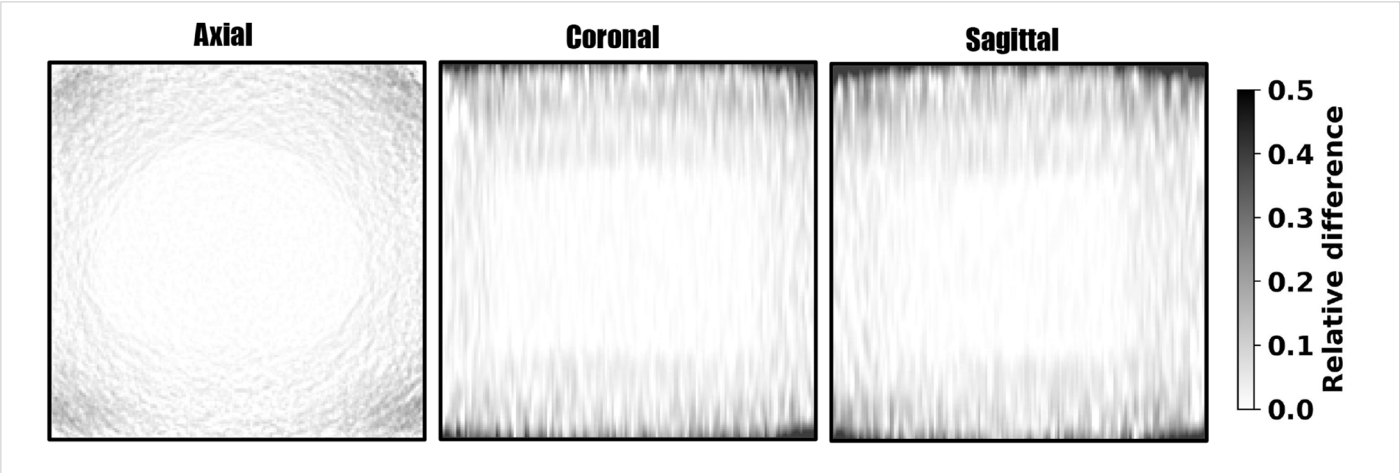

Fig. 6. Relative difference between non-random corrected and random corrected images of the NEMA IQ phantom scan, showing the proportion of random coincidences (contributing to the background) removed by the correction process.

Scatter Correction

After estimating the scatter contribution for each LOR and TOF bin, this information was incorporated into the CASToR list-mode file and the images were reconstructed using the same parameters specified in the image reconstruction section. Fig. 7. presents the non-scatter-corrected and scatter-corrected images, showing that scatter correction improved the lung insert clearance along the line profile shown in the figure by 55.53%, and effectively removed the activity in the plastic layer positioned just above and below the phantom, as seen in the coronal and sagittal section of the images.

DISCUSSION

In this study we developed the first data correction framework for the first PET scanner based on plastic scintillator strips. The CT-based attenuation correction method enabled a more even activity distribution in the warm compartment of the NEMA IQ phantom and could successfully remove typical attenuation--related edge artifacts at the boundaries of the phantom. In the reconstructed images a large part of the activity concentration lost due to attenuation could be recovered.

The contribution of random events to the image data was about 18%. We implemented a first random-correction approach based on the delayed window method and used a variance reduction method to increase statistical significance of the randoms estimate by combining pseudo-crystals to detector blocks. As depicted in Fig. 6., the corrections removed up to 50% of the background activity concentration, while the remaining activity can be mostly attributed to scattered coincidences. Despite these efforts, the randoms estimate still suffer from the fairly low sensitivity of J-PET and therefore low statistics, which is why a more elaborate randoms correction method is currently under development. Having a reliable randoms correction method at hand will become beneficial once a long axial field-of-view version of the J-PET scanner with higher sensitivity has been developed.

Finally, the developed scatter correction method showed good success in removing unwanted activity from the cold plastic parts in the NEMA IQ phantom and considerably reducing the activity concentration inside the cold lung insert. Residual activity inside the lung insert could be due to low statistics in the number of collected events and spillover due to limited spatial resolution. However, the activity could potentially be further reduced by increasing the measurement time, refining reconstruction parameters and optimizing the scaling of the simulated scatter sinograms. Another limitation could originate from the scintillator material implemented in the MC tool SimSET. To increase the sensitivity in the simulation and due to the limited availability of materials in the SimSET data base, LYSO was simulated, which exhibited different attenuation properties for incoming gamma rays compared to plastic scintillators. The distribution of scattered events over the sinograms might be different and will require further research and optimization.

Additionally, the bottom edge of the phantom exhibits a concave shape after scatter has been corrected. Since the CT and PET scan of the phantom were performed on different scanner beds with the phantom being moved in between, PET-CT misalignments

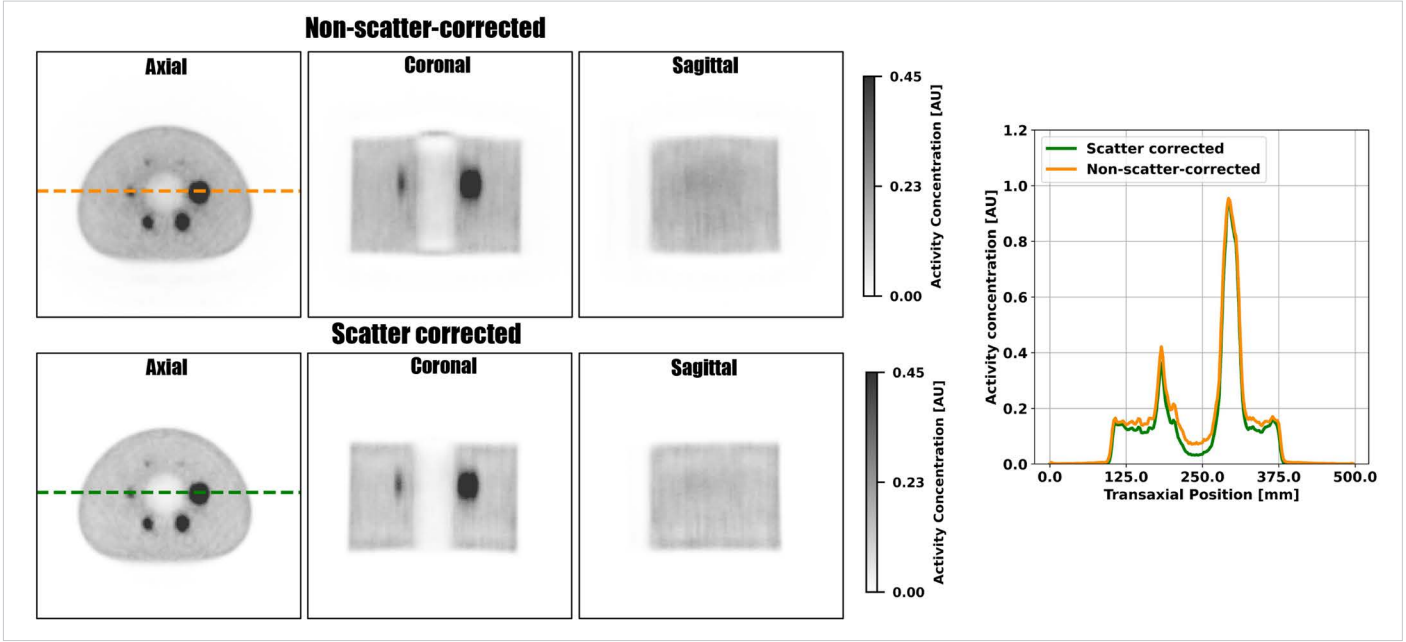

Fig. 7. Comparison of non-scatter-corrected (top) and scatter-corrected (bottom) images of the NEMA IQ phantom, alongside line profiles illustrating the effects of scatter correction. The non-scatter-corrected image shows reduced clearance in the lung insert region, with remaining activity clearly visible in the plastic layer visible above and below the phantom in both coronal and sagittal sections. In contrast, the scatter-corrected image demonstrates enhanced lung-insert clearance and effective removal of the activity in the plastic layers. The line profiles through the lung insert further emphasize the improved image quality after scatter correction.

could not be completely excluded. Also, the different physical properties of the PET- and CT-bed could contribute to inaccuracies in the correction for attenuation and scatter, and might explain the deformities in the phantom. Future work envisages meticulous phantom positioning and accurate PET-CT-alignment as well as similar bed-qualities for PET and CT imaging.

The qualitative results obtained with the modular J-PET for the NEMA IQ phantom demonstrate significant promise in enhancing image quality through the applied correction techniques. The reconstructed images reveal that, even with existing limitations, the applied correction techniques – such as scatter and random corrections – effectively enhance image quality.

The modular J-PET, built at Jagiellonian University, represents a pioneering effort in PET imaging with plastic scintillators. Unlike conventional PET systems, typically constructed with crystal--based detectors, the Modular J-PET utilizes plastic scintillators, marking a significant shift toward a more accessible and potentially cost-effective approach for PET technology. While this prototype exhibits limitations, particularly in terms of sensitivity and axial resolution, it demonstrates a crucial proof of concept, setting the stage for future advancements: by expanding the FOV and enhancing sensitivity and axial resolution, a total-body J-PET would enable high-quality imaging at lower cost [29]. This advancement would make total-body PET imaging more affordable and more accessible for many institutes around the world.

CONCLUSIONS

In this article we presented the first image of a NEMA image quality phantom obtained with the modular J-PET, incorporating all correction techniques. The qualitative results are promising and offer strong initial validation for these corrections. However, a thorough quantitative analysis is necessary to fully validate the effectiveness of these correction methods. Future research will focus on validating and implementing these correction techniques for human subject images obtained with the J-PET and on developing correction techniques for the total-body J-PET.

ACKNOWLEDGEMENTS

We acknowledge support from the National Science Centre of Poland through grants MAESTRO no. 2021/42/A/ST2/00423 (P.M.), OPUS no. 2021/43/B/ST2/02150 (P.M.), OPUS24+LAP no. 2022/47/I/NZ7/03112 (E.S.) and SONATA no. 2023/50/E/ST2/00574 (S.S.), the Ministry of Science and Higher Education through grant nos. SPUB/SP/490528/2021 (P.M.), IAL/SP/596235/2023 (P.M.), the SciMat and qLife Priority Research Areas budget under the program Excellence Initiative – Research University at Jagiellonian University (P.M. and E.S.), the Research Support Module as part of the Excellence Initiative – Research University program at Jagiellonian University (M.D.), NIH no. R01 CA249422 and NIH no. R01 CA275188.

FUNDING

We acknowledge support from the National Science Centre of Poland through grants MAESTRO no. 2021/42/A/ST2/00423 (P.M.), OPUS no. 2021/43/B/ST2/02150 (P.M.), OPUS24+LAP no. 2022/47/I/NZ7/03112 (E.S.) and SONATA no. 2023/50/E/ST2/00574 (S.S.), the Ministry of Science and Higher Education through grant nos. SPUB/SP/490528/2021 (P.M.) and IAL/SP/596235/2023 (P.M.), and the SciMat and qLife Priority Research Areas budget under the program Excellence Initiative – Research University at Jagiellonian University (P.M. and E.S.).

REFERENCES

1. Alavi A, Werner TJ, Stępień EŁ, Moskal P. Unparalleled and revolutionary impact of PET imaging on research and day to day practice of medicine. Bio-Algorithms and Med-Systems. 2021 Dec 1;17(4):203–12. doi: https://doi.org/10.1515/bams-2021-0186.
2. Vandenberghe S, Moskal P, Karp JS. State of the art in total body PET. EJNMMI Physics. 2020 May 25;7(1):1–33. doi: https://doi.org/10.1186/s40658-020-00290-2.
3. Moskal P, Stępień EŁ. Prospects and Clinical Perspectives of Total-Body PET Imaging using Plastic Scintillators. PET Clinics. 2020 Jul 29;15(4):439–52. doi: https://doi.org/10.1016/j.cpet.2020.06.009.
4. Karakatsanis NA, Nehmeh MH, Conti M, Bal G, González AJ, Nehmeh SA. Physical performance of adaptive axial FOV PET scanners with a sparse detector block rings or a checkerboard configuration. Phys. Med. Biol. [Internet]. 2022 Apr 26;67(10):105010. doi: https://doi.org/10.1088/1361-6560/ac6aa1.
5. Zhang Y, Wong WH. System Design Studies for a Low-cost High-resolution BGO PET with 1-meter Axial Field of View. J. Nucl. Med [Internet]. 2017;58(Suppl 1):221. Available from: https://jnm.snmjournals.org/content/58/supplement_1/221.
6. Vandenberghe S, Karakatsanis NA, Akl MA, Maebe J, Surti S, Dierckx RA, et al. The potential of a medium-cost long axial FOV PET system for nuclear medicine departments. EJNMMI. 2022 Sep 30;50(3):652–60. doi: https://doi.org/10.1007/s00259-022-05981-9.
7. Moskal P, Baran J, Bass S, Choiński J, Chug N, Curceanu C, et al. Positronium image of the human brain in vivo. Sci Adv. 2024 Sep 13;10(37). doi: https://doi.org/10.1126/sciadv.adp2840.
8. Moskal P, Niedźwiecki Sz, Bednarski T, Czerwiński E, Kapłon Ł, Kubicz E, et al. Test of a single module of the J-PET scanner based on plastic scintillators. Nucl. Instrum. Methods Phys. Res. A. 2014 Aug 10;764:317–21. doi: https://doi.org/10.1016/j.nima.2014.07.052.
9. Nelms AT. Graphs of the Compton Energy-Angle Relationship and the Klein-Nishina Formula from 10 KeV to 500 MeV. Phys. Today. 1954;7:18.
10. Pałka M, Strzempek P, Korcyl G, Bednarski T, Niedźwiecki Sz, Białas P, et al. Multichannel FPGA based MVT system for high precision time (20 ps RMS) and charge measurement. J. Instrum. 2017 Aug 1;12(08):P08001. doi: https://doi.org/10.1088/1748-0221/12/08/p08001.

11. Korcyl G, Hiesmayr BC, Jasinska B, Kacprzak K, Kajetanowicz M, Kisielewska D, et al. Evaluation of Single-Chip, Real-Time tomographic data processing on FPGA SOC devices. IEEE Trans Med Imaging. 2018 May 17;37(11):2526–35. doi: https://doi.org/10.1109/tmi.2018.2837741.
12. Ardebili FT, Niedźwiecki S, Moskal P. Evaluation of Modular J-PET sensitivity. Bio-Algorithms and Med-Systems. 2023 Dec 31;19(1):132–8. doi: https://doi.org/10.5604/01.3001.0054.1973.
13. Ardebili FT. Evaluation of the NEMA characteristics for the Modular J--PET scanner [thesis]. Krakow: Jagiellonian University; 2024.
14. Ardebili FT, Moskal P. Assessing the Spatial Resolution of the Modular J-PET Scanner using the Maximum-Likelihood Expectation-Maximization (MLEM) algorithm. Bio-Algorithms and Med-Systems. 2024 Nov 21;20(Special Issue):1–9. doi: https://doi.org/10.5604/01.3001.0054.8095.
15. Hoffman EJ, Huang SC, Phelps ME, Kuhl DE. Quantitation in positron emission computed tomography. J Comput Assist Tomogr. 1981 Jun 1;5(3):391–400. doi: https://doi.org/10.1097/00004728-198106000-00015.
16. Knoll GF. Radiation detection and Measurement. New York: Wiley; 1955.
17. Evans RD. The Atomic Nucleus. New York: McGraw Hill Book Co; 1955.
18. Brasse D, Kinahan PE, Lartizien C, Comtat C, Casey M, Michel C. Correction methods for random coincidences in fully 3D Whole-Body PET: Impact on data and image quality. J Nucl Med. 2005 May;46(5):859–67.
19. Oliver JF, Rafecas M. Modelling random coincidences in positron emission tomography by using singles and prompts: a comparison study. PLoS ONE. 2016 Sep 7;11(9):e0162096. doi: https://doi.org/10.1371/journal.pone.0162096.
20. Ollinger JM. Model-based scatter correction for fully 3D PET. Phys. Med. Biol. 1996 Jan 1;41(1):153–76. doi: https://doi.org/10.1088/0031-9155/41/1/012.
21. Levin CS, Dahlbom M, Hoffman EJ. A Monte Carlo correction for the effect of Compton scattering in 3-D PET brain imaging. IEEE Trans. Nucl. Sci. 1995 Aug 1;42(4):1181–5. doi: https://doi.org/10.1109/23.467880.
22. Zhang X, Zhou J, Cherry SR, Badawi RD, Qi J. Quantitative image reconstruction for total-body PET imaging using the 2-meter long EXPLORER scanner. Phys. Med. Biol. 2017 Feb 27;62(6):2465–85. doi: https://doi.org/10.1088/1361-6560/aa5e46.
23. Bayerlein R, Spencer BA, Leung EK, Omidvari N, Abdelhafez YG, Wang Q, et al. Development of a Monte Carlo-based scatter correction method for total-body PET using the uEXPLORER PET/CT scanner. Phys. Med. Biol. 2024 Jan 24;69(4):045033. doi: https://doi.org/10.1088/1361-6560/ad2230.
24. Carney JPJ, Townsend DW, Rappoport V, Bendriem B. Method for transforming CT images for attenuation correction in PET/CT imaging. Med. Phys. 2006 Mar 21;33(4):976–83. doi: https://doi.org/10.1118/1.2174132.
25. Merlin T, Stute S, Benoit D, Bert J, Carlier T, Comtat C, et al. CASToR: a generic data organization and processing code framework for multi--modal and multi-dimensional tomographic reconstruction. Phys. Med. Biol. 2018 Aug 16;63(18):185005. doi: https://doi.org/10.1088/1361-6560/aadac1.
26. Siddon RL. Fast calculation of the exact radiological path for a three-dimensional CT array. Med. Phys. 1985 Mar 1;12(2):252–5. doi: https://doi.org/10.1118/1.595715.
27. Badawi RD, Marsden PK. Developments in component-based normalization for 3D PET. Phys. Med. Biol. 1999 Jan 1;44(2):571–94. doi: https://doi.org/10.1088/0031-9155/44/2/020.
28. Pepin A, Stute S, Jan S, Comtat C. Normalization of Monte Carlo PET data using GATE. IEEE Nucl Sci Symp Conf Rec. 2011 Oct 1;4196–200. doi: https://doi.org/10.1109/nssmic.2011.6153804.
29. Moskal P, Kowalski P, Shopa RY, Raczyński L, Baran J, Chug N, et al. Simulating NEMA characteristics of the modular total-body J-PET scanner – an economic total-body PET from plastic scintillators. Phys. Med. Biol. 2021 Jul 21;66(17):175015. doi: https://doi.org/10.1088/1361-6560/ac16bd.